ACSNANO

www.acsnano.org

ARTICLE

Surfactant-Mediated Growth and Patterning of Atomically Thin Transition Metal Dichalcogenides

Xufan Li,[&] Ethan Kahn,[&] Gugang Chen, Xiahan Sang, Jincheng Lei, Donata Passarello, Akinola D. Oyedele, Dante Zakhidov, Kai-Wen Chen, Yu-Xun Chen, Shang-Hsien Hsieh, Kazunori Fujisawa, Raymond R. Unocic, Kai Xiao, Alberto Salleo, Michael F. Toney, Chia-Hao Chen, Efthimios Kaxiras, Mauricio Terrones, Boris I. Yakobson, and Avetik R. Harutyunyan*

Cite This: *ACS Nano* 2020, 14, 6570–6581

Read Online

ACCESS | Metrics & More | Article Recommendations | Supporting Information

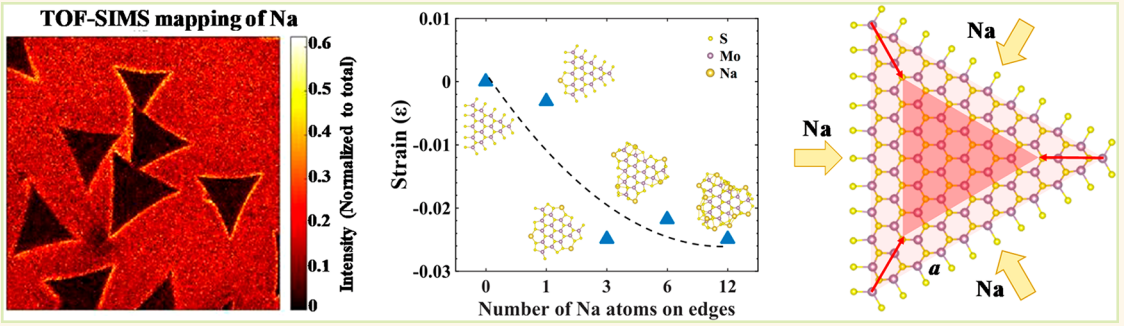

ABSTRACT: **The role of additives in facilitating the growth of conventional semiconducting thin films is well-established. Apparently, their presence is also decisive in the growth of two-dimensional transition metal dichalcogenides (TMDs), yet their role remains ambiguous. In this work, we show that the use of sodium bromide enables synthesis of TMD monolayers *via* a surfactant-mediated growth mechanism, without introducing liquefaction of metal oxide precursors. We discovered that sodium ions provided by sodium bromide chemically passivate edges of growing molybdenum disulfide crystals, relaxing in-plane strains to suppress 3D islanding and promote monolayer growth. To exploit this growth model, molybdenum disulfide monolayers were directly grown into desired patterns using predeposited sodium bromide as a removable template. The surfactant-mediated growth not only extends the families of metal oxide precursors but also offers a way for lithography-free patterning of TMD monolayers on various surfaces to facilitate fabrication of atomically thin electronic devices.**

KEYWORDS: *surfactant, MoS_2, edge passivation, strain, lithography-free patterning*

Single atomic layers of transition metal dichalcogenides (TMDs) are promising building blocks for developing fundamental science and applications.[1−6] However, materials processing and substrate selection pose great challenges as these extremely thin layers are vulnerable to any weak external perturbation, which can alter or impair their intrinsic properties. Therefore, it is of central importance for industrial-scale development to deeper understand the growth mechanism of two-dimensional (2D) TMD layers and thereby develop a facile synthesis method that allows growth on various surfaces with desirable patterns.

To control the growth and quality of thin films, modifying the surface energy of substrates and reducing the strain energy in the growing thin film using a foreign element has been a well-established strategy for the growth of conventional semiconductors.[7] The greatest example in the growth of conventional semiconducting thin films is the introduction of a mono/sublayer of a foreign species (*e.g.*, Sb) on the substrate (*e.g.*, Si(111)) prior to or during the growth of the semiconducting crystals (*e.g.*, Si, Ge). The foreign species is

Received: January 6, 2020
Accepted: April 27, 2020
Published: April 27, 2020

https://dx.doi.org/10.1021/acsnano.0c00132
ACS Nano 2020, 14, 6570–6581

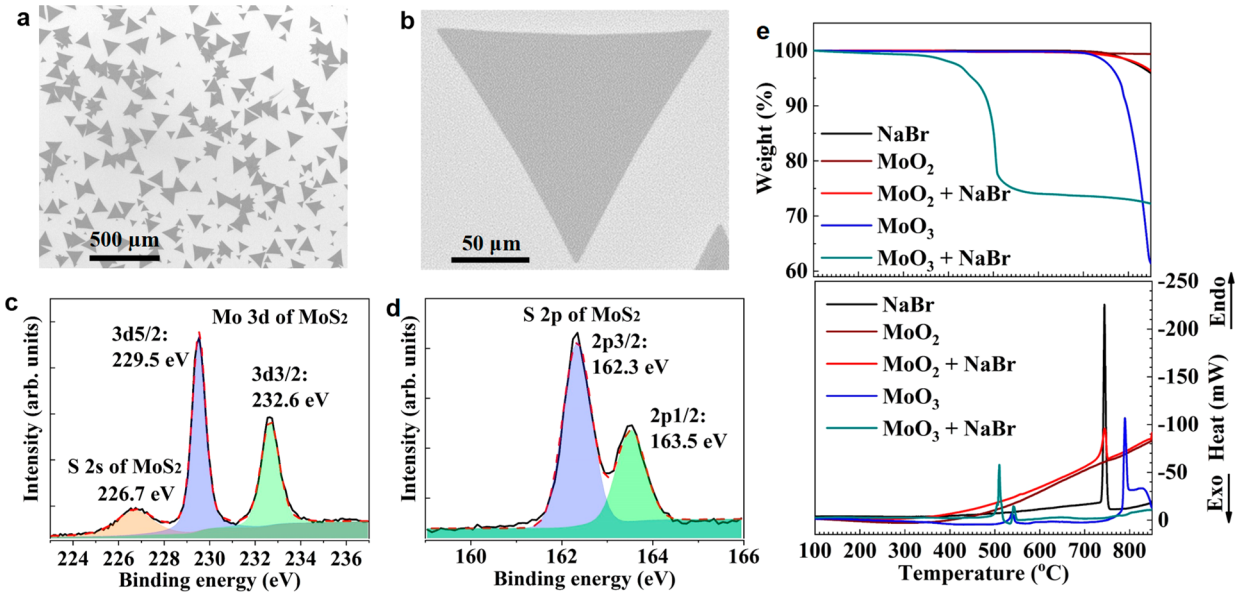

Figure 1. MoS_2 monolayers and thermogravimetric analysis (TGA)/differential scanning calorimetry (DSC) analysis of the precursors. (a) SEM image of MoS_2 monolayer flakes grown from MoO_2 on a SiO_2/Si substrate with predeposited NaBr. (b) Enlarged SEM image of a single-crystal monolayer with a lateral size of ~200 μm. (c,d) High-resolution XPS Mo 3d and S 2p scan from individual flakes, respectively, using a scanning X-ray source with a beam size of ~20 μm. (e) TGA (top) and DSC (bottom) curves for NaBr, MoO_2, MoO_2 + NaBr, MoO_3, and MoO_3 + NaBr.

called "surfactant", which enables a layer-by-layer (Frank−van der Merwe) growth mode at relatively high temperature without incorporating itself into the film.[8−11] This surfactant-mediated growth mechanism leads to thin films with high quality, making great impact on the conventional semiconductor industry.

Apparently, foreign elements (or additives) now play important roles in the growth of atomically thin TMDs, acting as nucleation seeds[12] or promoters that enable large monolayer crystals or domains,[12−16] reducing growth temperature, increasing metal precursor flux rate, improving crystallinity, and controlling crystalline phase.[14,17−19] Recently, Zhou *et al.* suggested a universal role of alkali metal salts in lowering melting point and leading to liquefaction of precursors, which is key to a "home-run" growth of two-dimensional metal chalcogenides including numerous combinations in the periodic table,[20] and the similar role has also been proposed in growing ribbon-like 2D MoS_2.[21] It has also been suggested that alkali metals, such as sodium, could serve as a catalyst in reducing the energy barrier to S attachment at a MoS_2 edge.[16] These investigations shed light on the growth mechanism of 2D TMDs and lead to great potential for scaling up the growth. However, at this point, taking into account the diversities of reported methods, it is hard to exclude other roles of additives in the growth of 2D TMDs. Advances in growth methods have also enabled big progress in device fabrication on atomically thin TMD layers.[22,23] However, these devices mainly rely on transferring TMD layers from the original substrate to a desired surface followed by e-beam or photolithography for proper patterning.[24−26] Developing alternative methods that allow direct patterned growth on desirable surfaces will advance device fabrication.

Here, we demonstrate a surfactant-mediated growth mechanism of TMD monolayer crystals of MX_2 (M = Mo, W; X = S, Se) on various substrates (*i.e.*, SiO_2, sapphire, and $SrTiO_3$) with predeposited sodium bromide (NaBr) additive, using metal dioxides (MoO_2, WO_2) as precursors instead of the widely used metal trioxides. We found that under our experimental conditions NaBr does not react with the dioxide precursors and, therefore, causes no liquefaction of the precursors in the growth process. The sodium ions that act as the surfactant chemically passivate the edges of the growing monolayer crystals, relaxing in-plane strains to suppress 3D islanding and promote monolayer growth. This surfactant-mediated growth mechanism does not require liquefaction and thereby enables growth from refractory metal dioxides. By taking that advantage, the predeposited NaBr was used as a removable template on the substrate, leading to a direct, lithography-free growth of a patterned MoS_2 monolayer.

RESULTS AND DISCUSSION

TMD crystals were grown on SiO_2/Si^{++} substrates using a chemical vapor deposition (CVD) method. In the growth, NaBr particles were first deposited on the substrate through thermal evaporation. Metal dioxides (*e.g.*, MoO_2, WO_2) were used as precursors, which were reacted with S or Se vapor at 770 °C (see Methods and Figure S1a for details). As shown in a scanning electron microscopy (SEM) image, the as-grown MoS_2 crystals are homogeneously triangle-shaped monolayers on the entire 1 × 1 cm^2 substrate, with lateral sizes ranging from 20 to 200 μm (Figure 1a,b; see Figure S1b−e, as well) and tunable edge morphologies (Figure S1f−i). As measured by conventional X-ray photoelectron spectroscopy (XPS) (Figure 1c,d) and micro-XPS (μ-XPS) using a synchrotron radiation source (Figure S2), the crystals are composed of Mo and S at an average Mo/S molar ratio of ~1:1.92, corresponding to MoS_2 with ~4% of sulfur vacancies, and no Na is detected from the basal plane of MoS_2 flakes (see Figure 2i). Raman and photoluminescence (PL) measurements prove the monolayer nature and high quality of the MoS_2 crystals (Figure S3). Similar characterization results were obtained for other TMD monolayers such as $MoSe_2$, WS_2, and WSe_2

https://dx.doi.org/10.1021/acsnano.0c00132
ACS Nano 2020, 14, 6570−6581

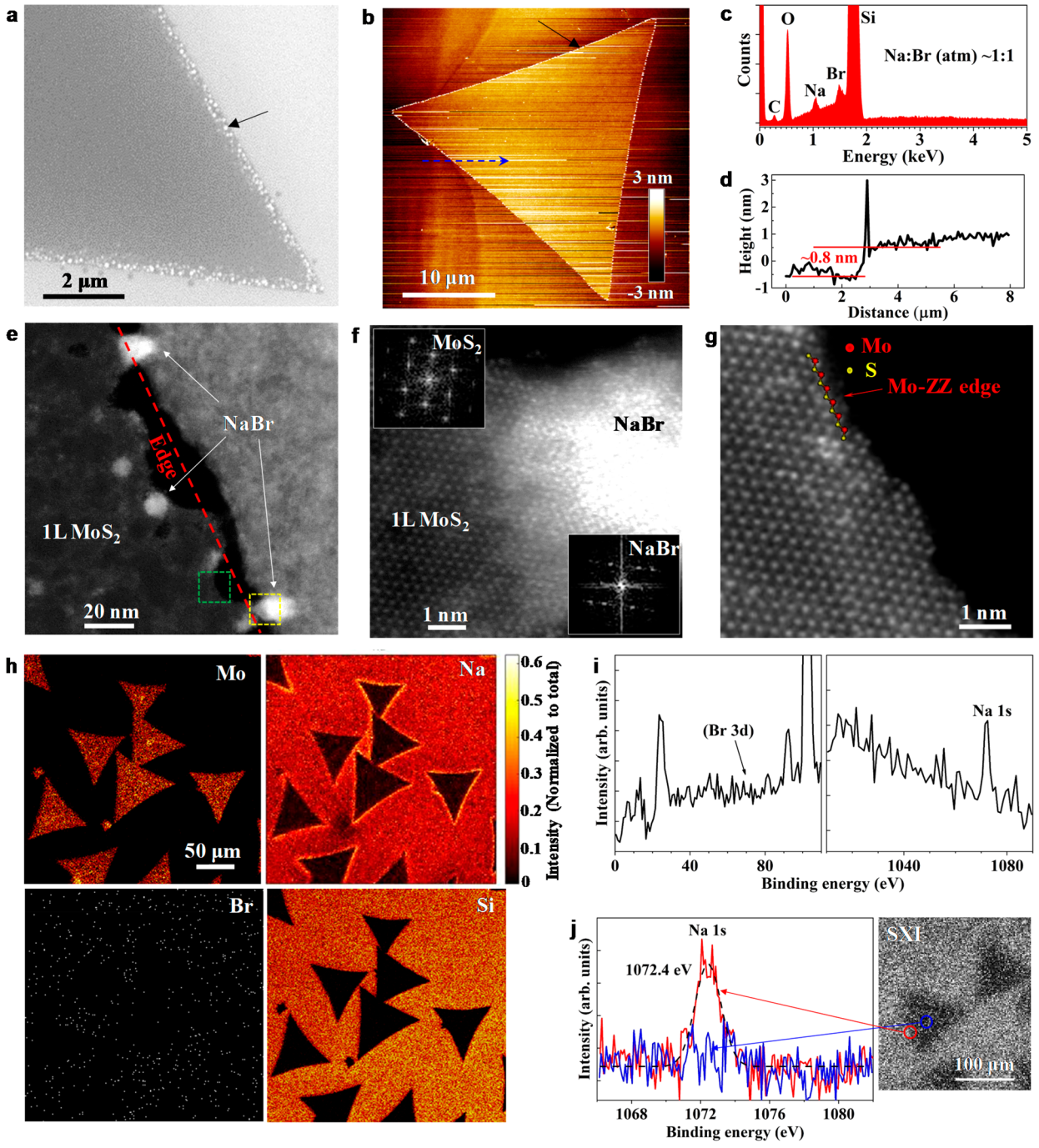

Figure 2. Edge passivation of MoS_2 monolayers (1L) by NaBr. (a) SEM image featuring NaBr particles (as indicated by the arrow) on the edges of a single-crystal MoS_2 monolayer grown for less than 5 min. (b) Atomic force microscopy (AFM) image of a single-crystal MoS_2 monolayer with NaBr nanoparticles (as indicated by the arrow) on the edges. (c) Energy-dispersive X-ray spectroscopy spectrum of the NaBr particles as indicated in (a). The atomic ratio of Na/Br is ~1:1, confirming that these particles are NaBr. (d) AFM height profile along the arrowed dashed blue line in (b) confirms the monolayer step height and shows the several nanometer-sized NaBr particles on the edge. (e) Scanning transmission electron microscopy (STEM) image showing a suspended edge area in a TEM grid with a quantifoil carbon film. The dashed red line indicates the edge of the monolayer. (f) Atomic resolution high-angle annular dark-field (HAADF)-STEM image acquired from the region inside the dashed yellow square in (e), featuring the MoS_2 monolayer and a NaBr nanoparticle attached to the edge. Insets show the corresponding fast Fourier transform images of the 1L MoS_2 and NaBr along their [001] zone axis, respectively. (g) Atomic resolution HAADF-STEM image of the region included by the dashed green square in (e), showing that the MoS_2 monolayer has a Mo-ZZ edge configuration. (h) Time-of-flight secondary ion mass spectrometry elemental mapping showing the distribution of Mo, Na, Br, and Si of typical MoS_2 monolayers grown on a SiO_2/Si substrate after 10 min annealing. Note that the Na^+ ion image is normalized to the total ion counts per pixel to verify its accumulation on the MoS_2 edges. (i) XPS survey on the whole area shown in the secondary X-ray image (SXI) in (j), with a beam size at ~200 μm, featuring binding energy of Br 3d and Na 1s. (j) High-resolution XPS Na 1s scans from the basal plane (blue curve) and the edge area (red curve) of an individual monolayer flake, corresponding to the blue and red circle, respectively, in the SXI (right) showing individual MoS_2 monolayer flakes. The beam size is ~20 μm.

https://dx.doi.org/10.1021/acsnano.0c00132
ACS Nano 2020, 14, 6570−6581

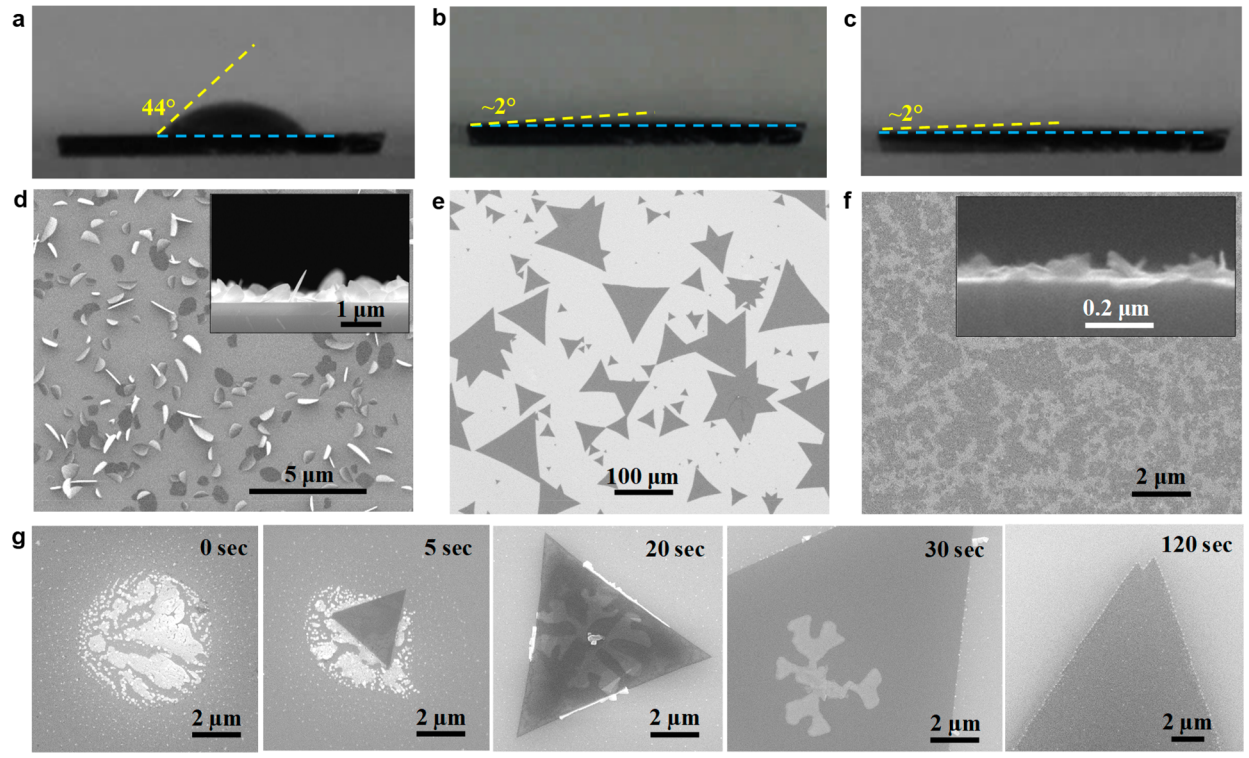

Figure 3. Surfactant-mediated growth of MoS_2 monolayers with NaBr. (a–c) Optical images of water droplets on SiO_2/Si substrate (a) untreated, (b) deposited with NaBr, and (c) washed by deionized water after NaBr deposition. (d–f) SEM images showing MoS_2 grown on the substrates shown in (a–c), respectively, from the MoO_2 precursor. Insets in (d) and (f) are corresponding cross-sectional SEM images. (g) SEM images showing growth stage at 0, 5, 20, 30, and 120 s for the MoS_2 monolayers on the SiO_2/Si substrate predeposited with NaBr. The image for 0 s shows only the NaBr.

(Figure S4). Importantly, we found that the presence of NaBr is mandatory for growing monolayer crystals; that is, without this additive, only vertically grown thick flakes with various aspect ratios were obtained on the substrate (see Figure 3d) or, in some cases, no growth at all. Apparently, NaBr assists the crystal nucleation and transits the three-dimensional (3D) islanding growth mode to 2D growth mode.

In order to understand the role of NaBr in the growth of TMD monolayers, we first conducted thermogravimetric analysis (TGA) and differential scanning calorimetry (DSC) measurement on precursors and their mixtures with NaBr under Ar flow (Figure 1e). NaBr shows an endothermic peak at ~750 °C, at which the weight starts to decrease significantly, corresponding to its melting point. No significant weight loss nor endothermic peak is observed for MoO_2 in the measurement temperature range due to its higher melting point (~1100 °C). The mixture of MoO_2 and NaBr shows their own independent thermogravimetric and calorimetric behavior, indicating no liquefaction of MoO_2 at the TMD growth temperature (*e.g.*, 770 °C) (Figure 1e and Figure S5a). In contrast, when MoO_3 is mixed with NaBr, a new endothermic peak shows up at ~500 °C on the DSC curve, together with a significant weight loss, corresponding to the liquefaction of MoO_3.[20,21] This liquefaction effect is in agreement with previous reports when MoO_3 was mixed with other salts (*e.g.*, NaCl).[20,21] Therefore, the TGA and DSC results indicate that, when MoO_2 is used as the precursor, the presence of NaBr does not change its melting temperature (similar phenomena for WO_2, as shown in Figure S5b). In addition, X-ray diffraction (XRD) and other elemental analysis results prove that MoO_2 does not react with NaBr to form new products when their mixture is heated or reacted with S vapor under the TMD growth condition (Figure S6). The above findings demonstrate that, instead of causing the liquefaction of trioxide precursors, NaBr should play a different role in the TMD growth when dioxides are used as the precursors.

Next, we identified the role of NaBr through a series of microscopic characterization techniques. We observed that for monolayer MoS_2 flakes grown for less than 5 min, NaBr nanoparticles remain accumulated on their edges, as revealed by SEM (Figure 2a, as indicated by a solid arrow) and energy-dispersive X-ray spectroscopy (EDS, Figure 2c), atomic force microscopy (AFM, Figure 2b,d), and scanning transmission electron microscopy (STEM, Figure 2e) analyses. The atomic resolution high-angle annular dark-field (HAADF)-STEM image (Figure 2f) clearly shows that a NaBr nanoparticle, also confirmed by the fast Fourier transform (FFT) pattern (inset of Figure 2f) as a face-centered cubic NaCl structure, attaches to the Mo-terminated zigzag (Mo-ZZ) monolayer edge (Figure 2g; see Figure S7, as well). These NaBr nanoparticles can be removed after a long annealing time (*e.g.*, >10 min; see Figure S8). After that, a nearly uniform Na signal was still observed across the SiO_2 substrate by using time-of-flight secondary ion mass spectrometry (TOF-SIMS), whereas Br was hardly detected (Figure 2h). Such an observation is also corroborated by XPS results (Figure 2i). More importantly, the Na signal significantly enhances along the edges of MoS_2 triangles, by more than two times compared with that on the substrate (Figure 2h). As the Na^+ signal is normalized to the total ion counts per pixel, such an enhancement could not be a topographical or a matrix effect but does come from a real accumulation of the Na^+ on the

https://dx.doi.org/10.1021/acsnano.0c00132
ACS Nano 2020, 14, 6570–6581

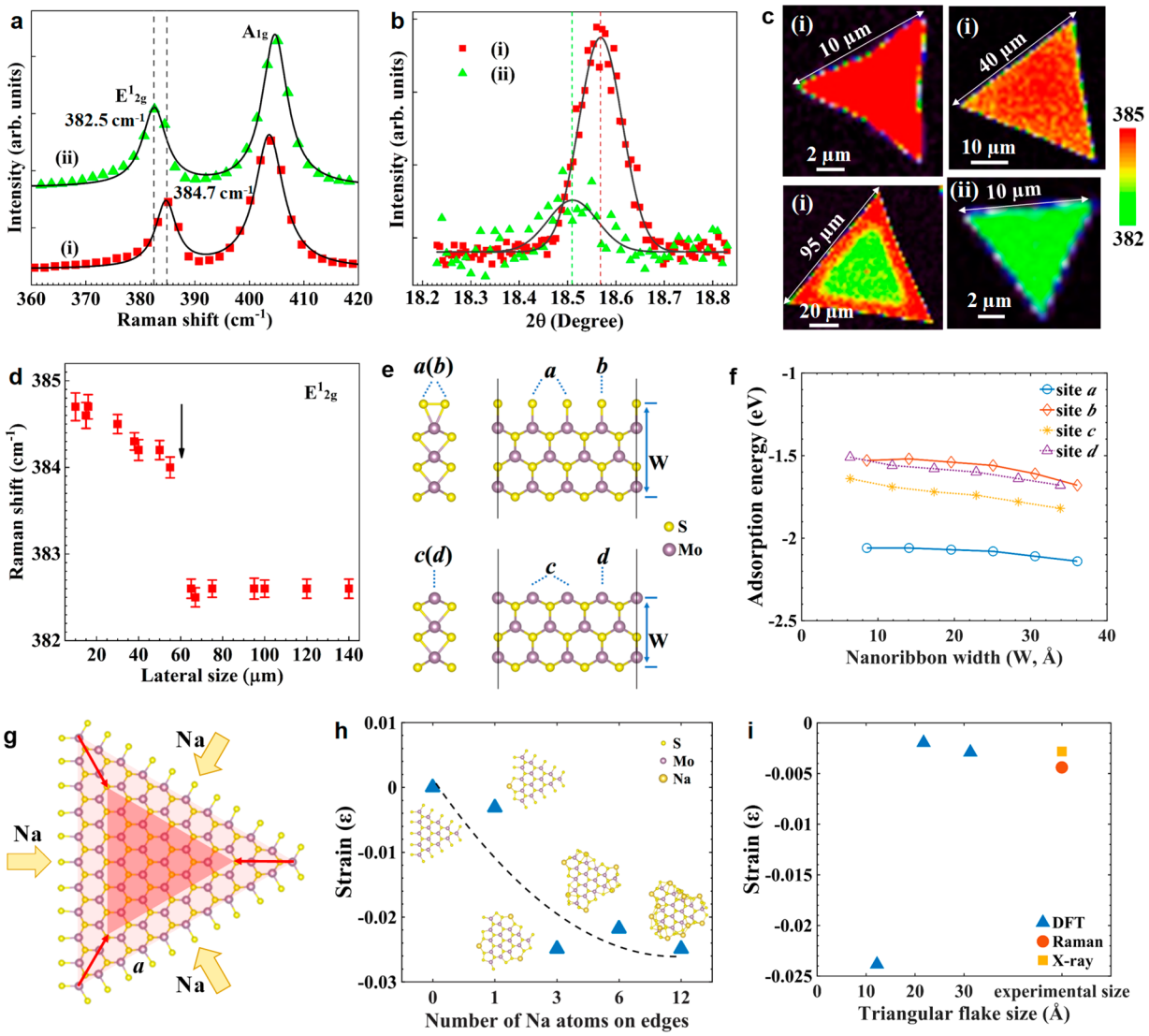

Figure 4. Effect of edge passivation by Na. (a) Raman spectra of MoS_2 monolayers (i) and (ii) with the same size of 10 μm. The scattered symbols are measured spectra, fitted by solid curves. Note that the spectra are offset for clarity. (b) High-resolution (10) diffraction peaks of monolayers (i) and (ii) (red and green scattered symbols, respectively) acquired using synchrotron X-ray diffraction. All peaks are well-fitted by Gaussian curves (solid lines). The apparent lower intensity from (ii) is due to a lower flake density on the substrate. (c) Raman E^1_{2g} energy mapping of a 10, 40, and 95 μm sized monolayer (i) and a 10 μm sized monolayer (ii). (d) Dependence of the E^1_{2g} energy on flake size of monolayers (i). Note that all of the spectra here were acquired from the central region of the flakes. (e) Top and side views of S-terminated Mo-ZZ edge (top) and Mo-ZZ edge (bottom). The possible Na adsorption sites are labeled *a*, *b*, *c* and *d*. (f) Adsorption energies of Na on S-terminated Mo-ZZ edge (solid lines, sites *a* and *b*) and Mo-ZZ edge (dotted lines, sites *c* and *d*). (g) Illustration of lattice shrinkage induced by Na adsorption at the edges. (h) Strain change (ε, change of the lattice constant *a*) as a function of Na concentration on the edges. The negative trend indicates reduction of tensile strain. (i) Strains at different flake sizes as calculated by density functional theory and measured by XRD.

edges. High-resolution XPS scan of Na 1s with a beam size of ~20 μm confirms that the Na signal was not detected from the basal plane but only from the edge areas of MoS_2 flakes and the substrate (Figure 2j). These results suggest that Na ions bond to the substrate and edges of MoS_2 monolayer flakes even though NaBr particles were removed after a long annealing time (theoretical calculation also shows ionic bonding between Na and MoS_2 edges as discussed below). It should be pointed out that, because it is hard to observe dangling Na atoms on the MoS_2 edges in STEM due to low contrast, thermal oscillation, electron-beam-induced transformation, and possible damage during the transfer process, we found that TOF-SIMS remains the most reliable way to show Na chemically passivating the MoS_2 edges. Such a passivation could possibly be the reason for changes in binding energy states of Mo and S at the edges in comparison to those on the basal plane, which was detected by μ-XPS with a beam size of 100 nm (Figure S2c–e).[27] Within this context, the above-observed 3D-to-2D growth mode transition could be attributed to two possible reasons: (1) alteration of the monolayer–substrate interfacial energy due to the Na ion adsorption on the substrate or (2) alteration of the formation energy of grown monolayers by Na passivation of the dangling bonds on edge atoms.

To explore these hypotheses, we first studied the influence on the growth of MoS_2 by alternating surface energy of the SiO_2/Si substrate, which was measured by the wettability of

https://dx.doi.org/10.1021/acsnano.0c00132
ACS Nano 2020, 14, 6570–6581

the substrate before (Figure 3a) and after NaBr deposition (Figure 3b). Indeed, the surface energy of the substrate has been changed with NaBr, and such a wettability change was not reversible even after the NaBr was washed away (Figure 3c), which is in agreement with the above-described XPS and TOF-SIMS observations. Subsequently, we used these three substrates (Figure 3a–c) to grow MoS_2 from the MoO_2 precursor. With the untreated SiO_2 (Figure 3a), as mentioned above, the growth resulted in 3D islands of MoS_2 with various aspect ratios (Figure 3d). With NaBr deposited on the substrate (Figure 3b), large-sized MoS_2 monolayer flakes were obtained (Figure 3e). However, after the NaBr was washed away, although the substrate was still highly wettable (Figure 3c), the growth resulted in a mixture of small, irregular monolayer domains with multilayers and islands on top (Figure 3f), similar to the Stranski–Krastanov growth mode.[28] These results indicate that the alteration of the substrate surface energy alone cannot cause the 3D-to-2D growth mode transition, and the presence of NaBr (more accurately Na ions) is indispensable to the MoS_2 monolayer growth. Indeed, with the predeposited NaBr on the substrate (Figure 3g, 0 s), the monolayer MoS_2 flakes initially nucleated and grew on top of the NaBr (Figure 3g, 5 s). Then, with increasing flake size, the NaBr migrates to and accumulates on the growth front or flake edges (Figure 3g, 20–120 s). This process is consistent with the result that Na passivating the edges of grown monolayer flakes and suggests that the monolayer growth is likely a surfactant-mediated process analogous to that in the growth of conventional semiconducting thin films as we mentioned above.[7−10] In the growth of conventional semiconducting thin films, the surfactant passivates the surface or terminates the edges of a grown layer and thereby amends the attachment/detachment rate of adatoms or reduces the strain energy accumulated in the growing film, respectively.[7−10] As a result, the presence of the surfactant ensures a smooth layer-by-layer growth and suppresses 3D islanding. In analogy, the passivation of the edges of MoS_2 monolayer flakes could play a similar role to sustain the growth confined in the 2D plane. The kinetics of this growth mechanism assumes a higher density of smaller flakes at lower synthesis temperatures, whereas there is a lower density of larger flakes at higher temperatures.[9] We examined such a rule in our MoS_2 monolayers grown at various temperatures from 700 to 850 °C, in which indeed the flake density decreases by orders of magnitude with increasing growth temperature, accompanied by the increase of average flake size (Figure S9). Moreover, it is observed that smaller flakes generally possess relatively rough edges (Figure S10), which is also another distinctive feature of the surfactant-mediated growth.[7]

In order to validate the second hypothesis and reveal the role of the Na ions bonded to the edges of MoS_2 monolayer flakes, we investigated the in-plane strain of the monolayer flakes. For comparison, we synthesized a control sample of MoS_2 monolayers from MoO_3 without using any promoter (named as sample (ii), whereas the monolayers grown from MoO_2 with predeposited NaBr on the substrate are named as sample (i)). Our Raman studies reveal obvious shifts of E^1_{2g} peak between these two different samples. For smaller-sized (<60 μm) flakes, the E^1_{2g} energy of (i) is ~2.2 cm^{-1} higher than that of (ii) (Figure 4a). According to previous studies,[29,30] such shifts have been attributed to the change of the in-plane strain, meaning that monolayers (i) have a lower strain than (ii). In order to verify this strain variation, we directly measured the lattice parameter a of MoS_2 monolayers (i) and (ii) (Figure S11) using X-ray diffraction with synchrotron radiation. The experiment was carried out on a 6-cycle diffractometer with a grazing incidence geometry to ensure enough signal intensity from monolayers.[31] Figure 4b shows high-resolution diffraction peaks from the monolayer (10) crystal plane. The peak positions correspond to a lattice constant a of 3.167 Å for flakes (i) with Na ions bonded to the edges and 3.176 Å for flakes (ii) grown from a MoO_3 precursor without any promoter, respectively (see Figure S12, as well). If the strain is defined as $\varepsilon = (a_{Na} - a_0)/a_0$, in which a_{Na} and a_0 stand for the lattice parameter with and without edge passivation by Na ions, the results indicate a 0.3% reduction of in-plane strain in flakes with edge passivation by Na ions. It is also found that the Raman E^1_{2g} mode energy is uniform within each smaller-sized (<60 μm) flake domain (Figure 4c, top), whereas as the flake size surpasses ~60 μm, the E^1_{2g} energy distribution in monolayers (i) becomes inhomogeneous, with a lower energy in the inner region (Figure 4c, bottom-left, Figure 4d, and Figure S13). This phenomenon suggests that, as the flake size gets larger, the strain relaxation effect gets weaker. As the flake grows to a certain size, the strain relaxation effect cannot be exerted on the central area of the flake, whereas the effect remains on the area close to the edges, which results in a strain discrepancy in the flake, as shown in Figure 4c. In contrast, the monolayers (ii) grown without surfactant show uniform higher strain even though the flake size is small (Figure 4c, bottom-right). Based on these results, the growth mechanism can be described as, during the growth, the surfactant (*i.e.*, Na ions) chemically passivates the edges of monolayer MoS_2 nuclei, relaxing in-plane strain, facilitating attachment, and limiting the detachment of adatoms from and to the edges and thereby suppressing 3D islanding while promoting 2D growth.[7−10]

The passivation of MoS_2 edges by Na ions was also confirmed by spin-polarized density functional theory (DFT) calculations, as implemented in the Vienna *ab initio* simulation package (VASP)[32] (see Methods). It has been reported that the most stable edge structure of the MoS_2 monolayer under typical (sulfur-rich) experimental conditions is the S-terminated Mo-ZZ edge (with dangling S atoms at the Mo-ZZ edge), for example, the a and b sites in Figure 4e. However, in most cases, the edge configurations observed in HAADF-STEM are Mo-ZZ, although in some isolated cases, S-terminated Mo-ZZ edges were imaged (Figures S7a and S8f). Possible reasons can be that the outermost S atoms are hard to identify in STEM images due to low contrast, or those dangling S atoms have been reconstructed under electron beam irradiation or removed during the transfer process for STEM. For comparison, we consider both S-terminated Mo-ZZ and Mo-ZZ edges for the adsorption of Na atoms. There are two possible adsorption sites for Na on the edges: sites a and b for the S-terminated Mo-ZZ edge and sites c and d for the Mo-ZZ edge (Figure 4e). On site a, the Na atom forms four bonds with the S atoms, in contrast to only two bonds on site b. As a result, the adsorption of Na on site a is ~0.53 eV stronger than that on site b (Figure 4f). Similarly, on site c, the adsorption of Na is stronger than that on d by ~0.13 eV. Bader charge analysis (see Methods) suggests that the bonding between the adsorbed Na and the edges is predominantly ionic. This is consistent with the experimental result, in which Na ions remain accumulated at the edges even after NaBr particles were evaporated after long annealing time (Figure

https://dx.doi.org/10.1021/acsnano.0c00132
ACS Nano 2020, 14, 6570–6581

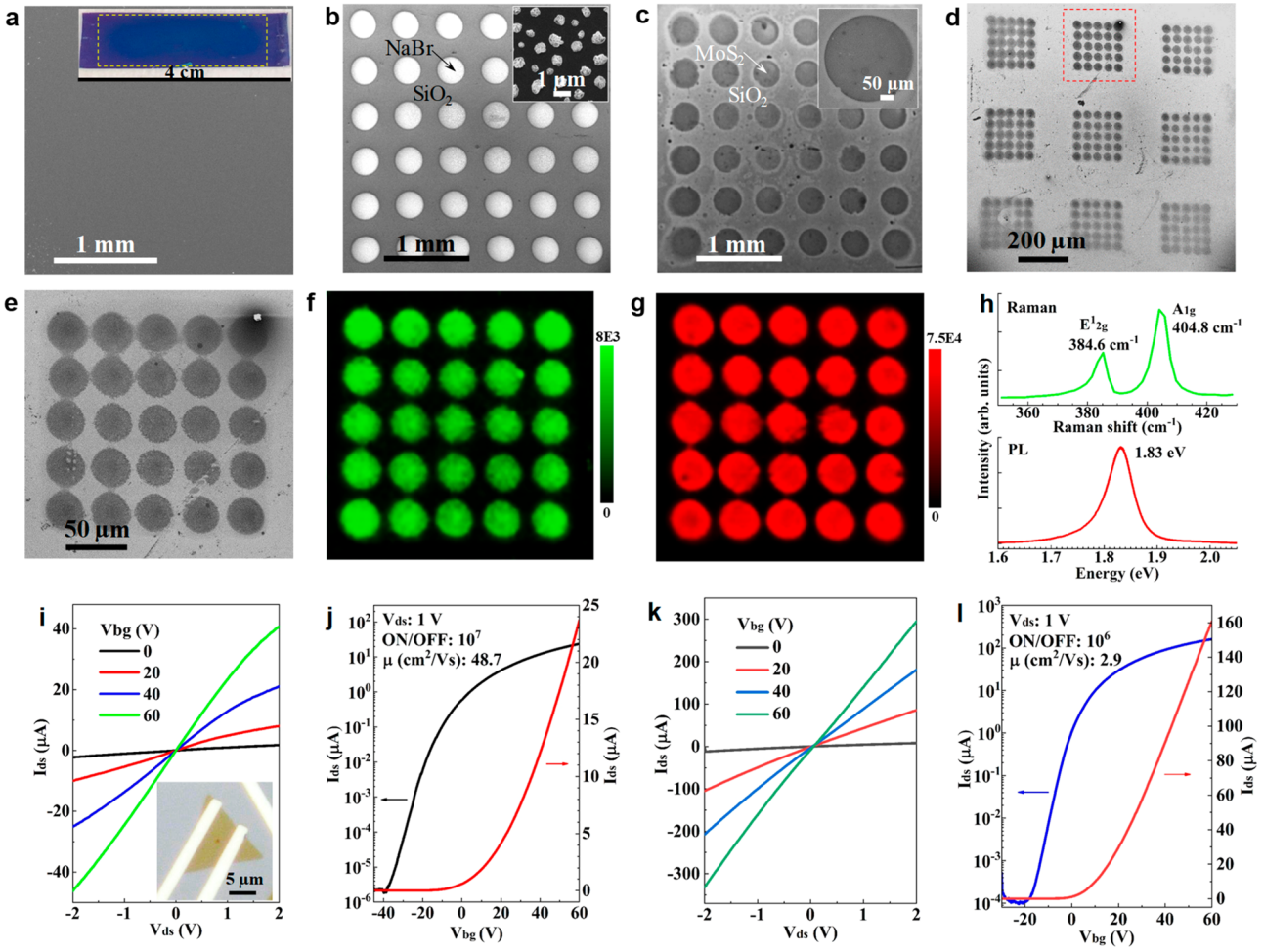

Figure 5. Large-area and patterned growth of MoS_2 monolayers with NaBr as templates and electrical properties. (a) SEM image of a centimeter-scale continuous MoS_2 monolayer film grown on a SiO_2/Si substrate predeposited with NaBr. Inset is the optical image of this ~4 × 1 cm^2 substrate, in which the region with blue contrast, as contained by the dashed rectangle, is the continuous monolayer film. (b) SEM image of a NaBr template deposited through a shadow mask with a 6 × 6 hole array on the SiO_2/Si substrate. Inset is the enlarged view of NaBr particles deposited through each hole. (c) SEM image of patterned MoS_2 grown using the NaBr layer in (b) as the template, showing a 6 × 6 array of monolayer disks. Inset is an enlarged SEM image of an individual polycrystalline MoS_2 monolayer disk. (d) SEM image of patterned MoS_2 monolayer disk arrays, with each monolayer disk being ~30 μm. (e) Enlarged image of the area in the dashed square in (d). (f,g) Raman (A_{1g}) and PL intensity mapping of the patterned MoS_2 monolayers shown in (e). (h) Corresponding Raman and PL spectra acquired from the MoS_2 monolayer disks. (i) Output curves of a single-crystal monolayer MoS_2 field-effect transistor (FET) device with a 5 μm channel length and a 5 μm channel width. Inset is the optical image of a typical device. (j) Corresponding transfer curve at V_{ds} = 1 V on both linear and logarithmic scale. (k) Output curves of a FET device based on a millimeter-scale polycrystalline monolayer MoS_2 pattern, with a 10 μm channel length and a 1000 μm channel width. See Figure S18a for the optical image of the corresponding device. (l) Corresponding transfer curve at V_{ds} = 1 V on both linear and logarithmic scale.

2g). The weaker Na adsorption (−1.18 eV) on a perfect MoS_2 surface (Figure S14 and Table S1) shows that the Na passivation of the edges is energetically more favorable. The calculated adsorption energy of the Na atom on the SiO_2 surface[33] (Figure S15) is −0.09 eV. The weak interaction between Na atoms and the SiO_2 surface serves as the basis for the floating of the NaBr underneath the MoS_2 flake to the growth front as observed in experiment (Figure 3g). Our calculation result also indicates that as the Na atom concentration increases on the edges of small MoS_2 monolayer crystals (~1 nm), the strain is notably relaxed (Figure 4h), and such a relaxation effect (reduction of Mo−Mo distance) is less prominent in larger flakes, which is consistent with experimental results (Figure 4i).

It should be noticed that, as Br was not detected being bonded to the edges of MoS_2 monolayers and only a very low amount of it remains on the substrate upon the evaporation of NaBr (in contrast to Na as proven by XPS and TOF-SIMS results), the role of the Br in this current work is not clear. Previous work suggested the formation of volatile metal oxyhalides (*i.e.*, MO_xBr_y).[14] However, these metal oxyhalides have a low melting point (<300 °C), and as no characteristic peaks appear on the TGA/DSC curves of MoO_2/WO_2 + NaBr mixtures below 300 °C (Figure 1e and Figure S5), we exclude this role under our experimental conditions. Similar results have been obtained when using NaCl as the additive to grow MoS_2 monolayers, in which Na is detected passivating monolayer edges and on the substrate, whereas Cl is hardly found (Figure S16).

Using NaBr as an additive and, consequently, Na ions as a surfactant, to mediate the growth of TMD monolayers enables controlled and scalable synthesis, which is of practical

https://dx.doi.org/10.1021/acsnano.0c00132
ACS Nano 2020, 14, 6570−6581

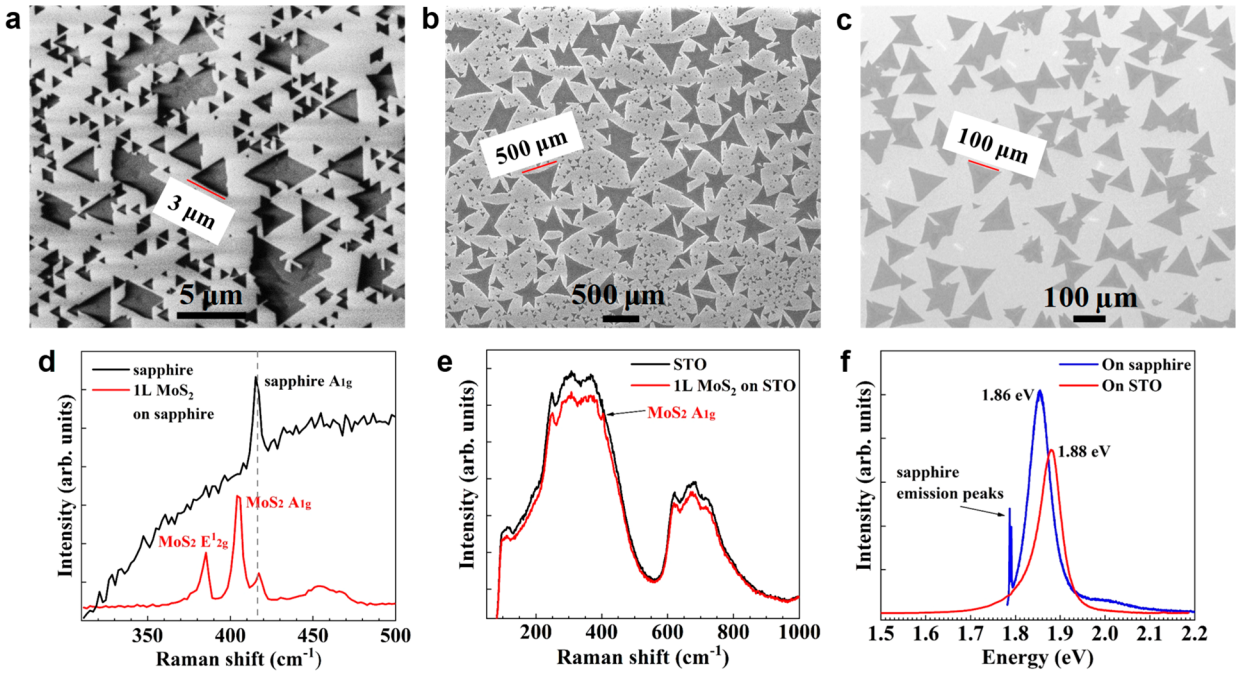

Figure 6. Surfactant-mediated growth of 1L MoS_2 on different substrates. (a,b) SEM images of MoS_2 monolayer flakes grown on a sapphire (001) substrate from MoO_2 without and with NaBr, respectively. (c) SEM images of MoS_2 monolayer flakes grown on a STO (001) substrate from MoO_2 with NaBr. (d) Raman spectra of sapphire (black curve) and MoS_2 monolayers (red curve) grown on it. (e) Raman spectra of STO (black curve) and MoS_2 monolayers (red curve) grown on it. (f) PL spectra of MoS_2 monolayer grown on the (001) surface of sapphire (blue curve) and STO (red curve).

significance. First, a centimeter-scale, uniform, continuous MoS_2 monolayer film (Figure 5a and Figure S17) was obtained by controlling the density of predeposited NaBr on the surface of a 4 × 1 cm^2 substrate (inset of Figure 5a). Moreover, NaBr can be deposited as patterned "templates" to grow MoS_2 monolayers in any desired pattern. For example, NaBr was first deposited through a stainless steel shadow mask with a 6 × 6 hole array (Figure 5b). The following growth of MoS_2 without the mask perfectly mimicked the pattern of the NaBr, forming a 6 × 6 array of polycrystalline monolayer disks (Figure 5c). Depending on the size of the voids on the shadow masks, we were able grow patterned MoS_2 monolayers with the feature size ranging from several millimeters (Figure S18) to ∼30 μm (Figure 5d,e), and the patterned MoS_2 monolayers show uniform and characteristic optical properties (Figure 5f–h and Figure S19). Hence, this demonstrates the use of salt as templates to fabricate various patterns of pristine MoS_2 monolayers without using lithographic processes, which is of great potential for electronics.

To measure the electrical properties, field-effect transistor (FET) devices were fabricated on both single-crystal MoS_2 monolayers (inset of Figure 5i) and patterned polycrystalline MoS_2 monolayers (Figure S20a) on their growth substrates using Si^{++} as the back gate electrode. The output (I_{ds}–V_{ds}) curves at different back-gate voltages (V_{bg}) indicate ohmic contacts between electrodes and the MoS_2 monolayer (Figure 5i,k). The transfer curve of the single-crystal device shows characteristic n-type behavior of MoS_2, with an ON/OFF ratio of 10^7 (Figure 5j). The single-crystal devices show carrier mobility (μ) of 21.5–48.7 $cm^2/(V\ s)$ out of 10 FET devices measured (Figure S20b), comparable to high-quality CVD-grown MoS_2 monolayers with a Si^{++} back-gate FET configuration.[16,34] In order to examine the electrical properties of millimeter-scale MoS_2 monolayers, we grew a triangular-patterned, continuous MoS_2 monolayer film with an average single-crystal domain size of ∼20 μm (Figure S18). The output current of this millimeter-scale FET device is an order of magnitude higher than the single-crystal one (Figure 5k), whereas the ON/OFF ratio is at 10^6 (Figure 5l) and the mobility is typically 0.6–2.9 $cm^2/(V\ s)$ (Figure S20b) with different pairs of electrodes measured (Figure S20a). These values are also comparable to previously reported polycrystalline MoS_2 monolayers[34] and could be enhanced with optimized device fabrication processes.[35]

The surfactant-mediated growth of MoS_2 monolayers was also conducted on a variety of substrates other than SiO_2/Si, such as the (001) plane of sapphire and $SrTiO_3$ (STO) (Figure 6). The growth from MoO_2 without NaBr resulted in well-aligned MoS_2 monolayer flakes on the sapphire (001) plane with a crystal size of up to ∼3 μm (Figure 6a), whereas the predeposited NaBr dramatically boosted the single crystal size up to ∼500 μm (Figure 6b). Large-sized (up to ∼100 μm) MoS_2 monolayer single crystals were also grown on STO (001) with the assistance of NaBr (Figure 6c). Characteristic Raman (Figure 6d,e) and PL (Figure 6f) spectra confirm the monolayer nature of the MoS_2 crystals through the surfactant-mediated growth on the (001) plane of sapphire and STO. The results indicate that the Na surfactant boosts the growth of MoS_2 on the (001) surface of sapphire and STO. However, we realize that the Na surfactant is not the universal one and does not always act as a crystal size booster, and it can even hinder growth of MoS_2 on some substrates, such as HOPG (highly oriented pyrolytic graphite) (Figure S21). Therefore, growth of high-quality, large-sized, single-crystal monolayers requires a combination of an appropriate surfactant and substrate for a given composition of TMD. To choose the combination requires a thorough investigation on the relationship between

https://dx.doi.org/10.1021/acsnano.0c00132
ACS Nano 2020, 14, 6570–6581

the adsorption energy of the surfactant to the substrate and that to the TMD monolayer.[7]

CONCLUSION

In summary, we presented the concept of surfactant-mediated growth of TMD monolayers that uses Na ion as a surfactant. We demonstrated the advantages of this growth mechanism in expanding the family of refractory metal oxides as growth precursors, adaptability on various types of substrates, and direct patterned growth to facilitate fabrication of atomically thin electronic devices with desirable configurations. However, with Na ion as the surfactant, there is still large limitations on the size and quality of the grown monolayers. According to the mechanism behind the surfactant-mediated growth of conventional semiconducting thin films, even though a proper surfactant was used and the layer-by-layer mode was promoted, it was impossible to completely remove the strain from the heteroepitaxial film, which was finally reduced by the introduction of dislocations in the grown film. Finding the best-matched surfactant, substrate, and the composition of growing material is essential to successful growth. This could also be true in the growth of 2D TMDs. In our TMD growth, with the growing size of the monolayers, the Na ion surfactant can only partially reduce the strain (*e.g.*, close to the edges). Therefore, searching for a surfactant−substrate−composition trio with the best match is a promising way to enable industrial-scale synthesis of 2D TMDs with high optical and electronic grades.

METHODS

Synthesis and Patterned Growth of Atomically Thin TMDs. The 2D TMDs were synthesized through a CVD method conducted in a tube furnace system equipped with a 1 in. quartz tube. The growth substrates, typically Si with 285 nm SiO_2 (SiO_2/Si) plates, were cleaned by acetone and isopropyl alcohol (IPA). About 0.5−2 mg of NaBr (Alfa Aesar, 99.99% metal basis) was loaded in a crucible and thermally evaporated and deposited on the substrate in vacuum (<10 mTorr). The substrate was placed face-down above an alumina crucible containing ∼1−3 mg powders of MoO_2 (Alfa Aesar, 99% metal basis) or WO_2 (Alfa Aesar, 99.9% metal basis), which was then inserted into the center of the quartz tube. Another crucible containing ∼50 mg S (Alfa Aesar, 99.5%) or Se (Alfa Aesar, 99.999% metal basis) powder was located at the upstream side of the tube, where a heating belt was wrapped. After the tube was evacuated to $\sim 5 \times 10^{-3}$ Torr, the reaction chamber pressure was increased to ambient pressure through 500 sccm argon gas flow. Then, the reaction was conducted at 770 °C (with a ramping rate of 40 °C/min) for 3−15 min with 60−120 sccm argon gas flow. For the growth of selenides, a 3−5 sccm flow of H_2 was also introduced. At 770 °C, the temperature at the location of S powder was ∼200 °C (∼450 °C for Se), as controlled by the heating belt. After growth, the heating belt was immediately removed, and the furnace was opened to allow a rapid cool down to room temperature with a fan. For patterned growth, the NaBr was first deposited on the substrate covered by a shadow mask (Photo Sciences Inc.) with certainly patterned voids, through a thermal evaporation and deposition process as described above. The density of the deposited particles was controlled by the amount of NaBr and deposition time. The substrate with specifically patterned NaBr particles was then placed in the CVD growth system described above for the growth of TMD monolayers under the same conditions as traditional growth except using pure oxides (*e.g.*, MoO_2 or WO_2) as precursors.

Characterization Methods. Morphologies of the as-synthesized 2D TMDs were characterized using SEM (FEI QUANTA FEG 650, operating at 20 kV) and AFM (Bruker Dimension Icon). The precursors before and after growth were studied using TGA/DSC (METTLER TOLEDO TGA/DSC 1 STAR^e system, operating at a heating rate of 5 °C/min under Ar protection) and in-house XRD (Bruker AXS D8 Advance A25 XRD, with Cu Kα, λ = 1.5418 Å). The optical properties of the 2D TMDs were studied using Raman and PL spectroscopy (Renishaw inVia Raman microscope, with 1800 grooves/mm grating and a 532 nm laser, 1 mW laser power, as excitation source). TOF-SIMS experiments were performed using a Physical Electronics nanoTOF II equipped 30 keV Bi_n^{q+} liquid-metal primary ion source filtered for the Bi_3^{++} ion. A compressed 6.5 ns primary ion pulse width was used, and an extraction voltage of 3026 V was applied to the sample stage. A primary ion dose of 1×10^{12} ions/cm^2 over an area of 100×100 μm^2 was used for data collection. XPS was conducted in a PHI VersaProbe III scanning XPS microprobe (Physical Electronics) with an aluminum X-ray anode and a microfocused scanning X-ray source. For large-area measurements, the X-ray beam size was ∼200 μm (power: ∼50 W), whereas for individual flakes, the beam size was ∼20 μm (power: ∼5 W). Auger electron spectroscopy (Figure S16) was conducted in a PHI 700 scanning Auger nanoprobe (Physical Electronics) at a working voltage and current of 5 kV and 10 nA, respectively.

The samples for STEM characterization were prepared using a typical wet transfer process. STEM images were acquired at 60 kV using a Nion UltraSTEM equipped with a probe aberration corrector (the convergence angle was 31 mrad). The inner and outer collection angles of the HAADF detector were 86 and 200 mrad, respectively. To enhance the signal-to-noise ratio, atomic resolution STEM images were blurred using a 2D Gaussian distribution.

The μ-XPS measurements were carried out at scanning photoelectron microscopy (SPEM) end-station located at beamline 09A1 of National Synchrotron Radiation Research Center, Taiwan. The SPEM system equipped with a Fresnel zone plate optical system to focus soft X-ray down to 100 nm spot size. The samples were annealed at 200 °C prior to the experiments under an ultrahigh vacuum condition. The photon energy was 400 eV for all μ-XPS measurements, which was calibrated by the Au 4f core level signal emitted from a clean gold foil electrically connected with the samples. To avoid charging effect, the MoS_2 flakes were grown on Si substrates with a 10 nm dry SiO_2 layer.

X-ray diffraction measurement was carried out at the Stanford Synchrotron Radiation Light-source (SSRL) on beamline 7-2, which is equipped with a 6-circle diffractometer. A Si(111) monochromated X-ray beam, with an energy of 14,009 eV, and focused to a spot size of 800×800 μm^2, was used for these measurements. The diffraction was detected by a Vortex detector positioned behind a set of 1 mrad soller slits. The diffraction pattern was collected at an incidence angle of 0.1°. To minimize the background from amorphous SiO_2, the MoS_2 flakes were grown on Si substrates with a 10 nm dry SiO_2 layer.

Computational Methods. Our spin-polarized first-principles calculations were performed using DFT in conjunction with the Perdew−Burke−Ernzerhof (PBE) generalized gradient approximation (GGA)[36] in the framework of the all-electron projector-augmented wave (PAW) method,[37] as implemented in VASP.[33] The energy cutoff was chosen to be 300 eV, and a $4 \times 4 \times 1$ supercell was constructed to represent the MoS_2 perfect surface. The Brillouin zones of MoS_2 supercell and nanoribbons were densely sampled with $3 \times 3 \times 1$ and $1 \times 3 \times 1$ k-points, respectively. For geometry optimization, a conjugate-gradient method was used to minimize the total energy and the forces acting on the ions until total energy was converged to 10^{-5} eV and the residual forces were less than 0.05 eV/Å. To avoid interactions between neighboring images, at least 10 Å vacuum space was added in the periodic directions.

The adsorption energy (E_{ad}) is used to evaluate the stability of the Na-adsorbed system, which is defined as

$$E_{ad} = E_{tot} - E_{MoS_2} - E_{Na}$$

where E_{tot} denotes the total energy of Na-adsorbed MoS_2 supercell or nanoribbon system, E_{MoS_2} is the total energy of the MoS_2 supercell or nanoribbon system without Na adsorption, and E_{Na} is the energy of an isolated Na atom in vacuum. Accordingly, a more negative adsorption

https://dx.doi.org/10.1021/acsnano.0c00132
ACS Nano 2020, 14, 6570−6581

energy indicates a more favorable exothermic adsorption process between MoS_2 and Na atoms. Bader charge analysis[38] was used to calculate charge transfer, which suggests that Na atom transfers 0.84|e| and 0.54−0.57|e| charge to S-terminated Mo-ZZ and Mo-ZZ edges, respectively, implying that the bonding between the adsorbed Na and the edges was predominantly ionic. We also calculated the adsorption of the Na atom on the SiO_2 surface as NaBr was predeposited on the substrate. The 2 × 2 reoptimized "dense" α-SiO_2 (001) surface was constructed to simulate the SiO_2/Si substrate as it was found to be 10% lower in energy than the well-known "dense" surface.[33]

Device Fabrication and Electrical Property Measurement. Electron beam lithography (FEI DB-FIB with Raith pattern writing software) was used for the device fabrication on single-crystal monolayer MoS_2. First, a layer of PMMA 495A4 was spin-coated on the SiO_2 (285 nm)/Si substrate with flakes followed by a 180 °C bake. After pattern writing and development, a 10 nm layer of Ti followed by a 50 nm layer of Au was deposited using electron beam evaporation. Finally, well-defined source and drain electrodes were revealed using a lift-off process with acetone/IPA. For large-scale patterned monolayer MoS_2, electrical contacts were fabricated using a photolithography process. The electrical properties of the devices were measured in vacuum (~10^{-6} Torr) in a probe station using a semiconductor analyzer (Keithley 4200). The mobility (μ) was calculated from the equation: $\mu = (L/WC_{ox})\times(\Delta G/\Delta V_{bg})$, where L is the channel length, W is the channel width, $G = I_{ds}/V_{ds}$ and $C_{ox} = 1.26 \times 10^{-8}$ F/cm^2 (the capacitance between channel and the back gate per unit area, $C_{ox} = \varepsilon_0\varepsilon_r/d_{ox}$, $\varepsilon_0 = 8.85 \times 10^{-12}$ F/m, $\varepsilon_r = 3.9$, and $d_{ox} = 285$ nm).

ASSOCIATED CONTENT

Supporting Information

The Supporting Information is available free of charge at https://pubs.acs.org/doi/10.1021/acsnano.0c00132.

Supporting figures and tables containing contents including morphologies and optical properties of MoS_2 monolayer flakes; μ-XPS measurement; studies on edge morphologies and structures; analyses on precursors; growth of other TMDs; details of strain measurement using Raman and synchrotron XRD; theoretical calculation on Na passivating monolayer edges; AES measurement on MoS_2 monolayer flakes grown using NaCl as additive; additional information on large-area continuous MoS_2 monolayers, device performance, and growth on HOPG substrate (PDF)

AUTHOR INFORMATION

Corresponding Author

Avetik R. Harutyunyan − *Honda Research Institute USA Inc., San Jose, California 95134, United States;* Email: aharutyunyan@honda-ri.com

Authors

Xufan Li − *Honda Research Institute USA Inc., San Jose, California 95134, United States;* orcid.org/0000-0001-9814-0383

Ethan Kahn − *Honda Research Institute USA Inc., San Jose, California 95134, United States; Department of Physics, The Pennsylvania State University, University Park, Pennsylvania 16802, United States*

Gugang Chen − *Honda Research Institute USA Inc., San Jose, California 95134, United States;* orcid.org/0000-0003-3798-320X

Xiahan Sang − *Center for Nanophase Materials Sciences, Oak Ridge National Laboratory, Oak Ridge, Tennessee 37831, United States*

Jincheng Lei − *Department of Materials Science and Nano Engineering, Rice University, Houston, Texas 77005, United States*

Donata Passarello − *Stanford Synchrotron Radiation Light Source, SLAC National Accelerator Laboratory, Menlo Park, California 94025, United States*

Akinola D. Oyedele − *Center for Nanophase Materials Sciences, Oak Ridge National Laboratory, Oak Ridge, Tennessee 37831, United States*

Dante Zakhidov − *Department of Materials Science and Engineering, Stanford University, Stanford, California 94305, United States;* orcid.org/0000-0003-3107-104X

Kai-Wen Chen − *National Synchrotron Radiation Research Center (NSRRC), Hsinchu 30076, Taiwan*

Yu-Xun Chen − *National Synchrotron Radiation Research Center (NSRRC), Hsinchu 30076, Taiwan*

Shang-Hsien Hsieh − *National Synchrotron Radiation Research Center (NSRRC), Hsinchu 30076, Taiwan*

Kazunori Fujisawa − *Department of Physics, The Pennsylvania State University, University Park, Pennsylvania 16802, United States*

Raymond R. Unocic − *Center for Nanophase Materials Sciences, Oak Ridge National Laboratory, Oak Ridge, Tennessee 37831, United States;* orcid.org/0000-0002-1777-8228

Kai Xiao − *Center for Nanophase Materials Sciences, Oak Ridge National Laboratory, Oak Ridge, Tennessee 37831, United States;* orcid.org/0000-0002-0402-8276

Alberto Salleo − *Department of Materials Science and Engineering, Stanford University, Stanford, California 94305, United States*

Michael F. Toney − *Stanford Synchrotron Radiation Light Source, SLAC National Accelerator Laboratory, Menlo Park, California 94025, United States;* orcid.org/0000-0002-7513-1166

Chia-Hao Chen − *National Synchrotron Radiation Research Center (NSRRC), Hsinchu 30076, Taiwan;* orcid.org/0000-0003-1311-8342

Efthimios Kaxiras − *Department of Physics, Harvard University, Cambridge, Massachusetts 02138, United States*

Mauricio Terrones − *Department of Physics, The Pennsylvania State University, University Park, Pennsylvania 16802, United States;* orcid.org/0000-0003-0010-2851

Boris I. Yakobson − *Department of Materials Science and Nano Engineering, Rice University, Houston, Texas 77005, United States*

Complete contact information is available at: https://pubs.acs.org/10.1021/acsnano.0c00132

Author Contributions

[&]X.L. and E.K. contributed equally.

Notes

The authors declare no competing financial interest.

ACKNOWLEDGMENTS

We thank Jordan Lerach and Sebastian Van Nuffel for assisting TOF-SIMS experiments, Tianyi Zhang and Ana Laura Elias for TEM measurements, Brian Tackett for XPS measurement, Gamini Sumanasekera for providing SiO_2/Si^{++} substrates with various thickness of oxide layers, and Jesse Sun-Woo Ko and Maria Lukatskaya for assisting with some of SEM measurements. STEM characterization and FET fabrication/measurement were conducted at the Center for Nanophase Materials

Sciences, which is a DOE Office of Science User Facility. The research using Stanford Synchrotron Radiation Light Source at SLAC National Accelerator Laboratory is supported by U.S. Department of Energy, Office of Science, Basic Energy Sciences under Contract No. DE-AC02-76SF00515. E.K. is funded by the Center for Integrated Quantum Materials, NSF Grant No. DMR-1231319, and by ARO MURI Award No. W911NF-14-0247. D.Z. is supported by the National Science Foundation Graduate Research Fellowship under Grant No. DGE-1656518. AES. and conventional XPS measurements were performed at the Stanford Nano Shared Facilities (SNSF), supported by the National Science Foundation under Award No. ECCS-1542152.

REFERENCES

(1) Wu, S.; Fatemi, V.; Gibson, Q. D.; Watanabe, K.; Taniguchi, T.; Cava, R. J.; Jarillo-Herrero, P. Observation of the Quantum Spin Hall Effect up to 100 K in a Monolayer Crystal. *Science* **2018**, *359*, 76−79.
(2) Xia, F.; Wang, H.; Xiao, D.; Dubey, M.; Ramasubramaniam, A. Two-Dimensional Material Nanophotonics. *Nat. Photonics* **2014**, *8*, 899−907.
(3) Xu, X.; Yao, W.; Xiao, D.; Heinz, T. F. Spin and Pseudospins in Layered Transition Metal Dichalcogenides. *Nat. Phys.* **2014**, *10*, 343−350.
(4) Sie, E. J.; Lui, C. H.; Lee, Y.-H.; Fu, L.; Kong, J.; Gedik, N. Large, Valley-Exclusive Bloch-Siegert Shift in Monolayer WS_2. *Science* **2017**, *355*, 1066−1069.
(5) Mak, K. F.; He, K.; Lee, C.; Lee, G. H.; Hone, J.; Heinz, T. F.; Shan, J. Tightly Bound Trions in Monolayer MoS_2. *Nat. Mater.* **2013**, *12*, 207−211.
(6) Low, T.; Chaves, A.; Caldwell, J. D.; Kumar, A.; Fang, N. X.; Avouris, P.; Heinz, T. F.; Guinea, F.; Martin-Moreno, L.; Koppens, F. Polaritons in Layered Two-Dimensional Materials. *Nat. Mater.* **2017**, *16*, 182−194.
(7) Markov, I. V. *Crystal Growth for Beginners. Fundamentals of Nucleation, Crystal Growth and Epitaxy*, 2nd ed.; World Scientific Publishing: Singapore, 2003; p 494.
(8) Copel, M.; Reuter, M. C.; Kaxiras, E. R.; Tromp, M. Surfactants in Epitaxial Growth. *Phys. Rev. Lett.* **1989**, *63*, 632.
(9) Kandel, D.; Kaxiras, E. The Surfactant Effect in Semiconductor Thin Film Growth. *Solid State Phys.* **2000**, *54*, 219−262.
(10) Fong, C. Y.; Watson, M. D.; Yang, L. H.; Ciraci, S. Surfactant-Mediated Growth of Semiconductor Materials. *Modelling Simul. Mater. Sci. Eng.* **2002**, *10*, R61−R77.
(11) Portavoce, A.; Berbezier, I.; Ronda, A. Sb-Surfactant-Mediated Growth of Si and Ge Nanostructures. *Phys. Rev. B: Condens. Matter Mater. Phys.* **2004**, *69*, 155416.
(12) Ling, X.; Lee, Y. − H.; Lin, Y.; Fang, W.; Yu, L.; Dresselhaus, M. S.; Kong, J. Role of the Seeding Promoter in MoS2 Growth by Chemical Vapor Deposition. *Nano Lett.* **2014**, *14*, 464−472.
(13) Kim, H.; Ovchinnikov, D.; Deiana, D.; Unuchek, D.; Kis, A. Suppressing Nucleation in Metal-Organic Chemical Vapor Deposition of MoS_2 Monolayers by Alkali Metal Halides. *Nano Lett.* **2017**, *17*, 5056−5063.
(14) Li, S.; Wang, S.; Tang, D. − M.; Zhao, W.; Xu, H.; Chu, L.; Bando, Y.; Golberg, D.; Eda, G. Halide-Assisted Atmospheric Pressure Growth of Large WSe_2 and WS_2 Monolayer Crystals. *Appl. Mater. Today* **2015**, *1*, 60−66.
(15) Chen, K.; Chen, Z.; Wan, X.; Zheng, Z.; Xie, F.; Chen, W.; Gui, X.; Chen, H.; Xie, W.; Xu, J. A Simple Method for Synthsis of High-Quality Millimeter-Scale 1T' Transition-Metal Telluride and Near-Field Nanooptical Properties. *Adv. Mater.* **2017**, *29*, 1700704.
(16) Yang, P.; Zou, X.; Zhang, Z.; Hong, M.; Shi, J.; Chen, S.; Shu, J.; Zhao, L.; Jiang, S.; Zhou, X.; Huan, Y.; Xie, C.; Gao, P.; Chen, Q.; Zhang, Q.; Liu, Z.; Zhang, Y. Batch Production of 6-Inch Uniform Monolayer Molybdenum Disulfide Catalyzed by Sodium in Glass. *Nat. Commun.* **2018**, *9*, 979.
(17) Liu, L.; Wu, J.; Wu, L.; Ye, M.; Liu, X.; Wang, Q.; Hou, S.; Lu, P.; Sun, L.; Zheng, J.; Xing, L.; Gu, L.; Jiang, X.; Xie, L.; Jiao, L. Phase-Selective Synthesis of 1T' MoS_2 Monolayers and Heterophase Bilayers. *Nat. Mater.* **2018**, *17*, 1108−1114.
(18) Barreau, N.; Bernède, J. C. MoS_2 Textured Films Grown on Glass Substrates through Sodium Sulfide Based Compounds. *J. Phys. D: Appl. Phys.* **2002**, *35*, 1197−1204.
(19) Gourmelon, E.; Bernede, J. C.; Pouzet, J.; Sørensen, G. Photoconductive MoS_2 Thin Films Obtained at Low Temperature (T < 865 K). *Phys. Status Solidi - Rapid Res. Lett.* **1997**, *161*, R5−R6.
(20) Zhou, J.; Lin, J.; Huang, X.; Zhou, Y.; Chen, Y.; Xia, J.; Wang, H.; Xie, Y.; Yu, H.; Lei, J.; Wu, D.; Liu, F.; Fu, Q.; Zeng, Q.; Hsu, C.-H.; Yang, C.; Lu, L.; Yu, T.; Shen, Z.; Lin, H.; et al. A Library of Atomically Thin Metal Chalcogenides. *Nature* **2018**, *556*, 355−359.
(21) Li, S.; Lin, Y. − C.; Zhao, W.; Wu, J.; Wang, Z.; Hu, Z.; Shen, Y.; Tang, D. − M.; Wang, J.; Zhang, Q.; Zhu, H.; Chu, L.; Zhao, W.; Liu, C.; Sun, Z.; Taniguchi, T.; Osada, M.; Chen, W.; Xu, Q. − H.; Wee, A. T. S.; et al. Vapour-Liquid-Solid Growth of Monolayer MoS_2 Nanoribbons. *Nat. Mater.* **2018**, *17*, 535−542.
(22) Radisavljevic, B.; Radenovic, A.; Brivio, J.; Giacometti, V.; Kis, A. Single-Layer MoS_2 Transistors. *Nat. Nanotechnol.* **2011**, *6*, 147−150.
(23) Nourbakhsh, A.; Zubair, A.; Sajjad, R. N.; Tavakkoli K. G., A.; Chen, W.; Fang, S.; Ling, X.; Kong, J.; Dresselhaus, M. S.; Kaxiras, E.; Berggren, K. K.; Antoniadis, D.; Palacios, T. MoS_2 Field-Effect Transisitor with Sub-10 nm Channel Length. *Nano Lett.* **2016**, *16*, 7798−7806.
(24) Sangwan, V. K.; Lee, H. − S.; Bergeron, H.; Balla, I.; Beck, M. E.; Chen, K. − S.; Hersam, M. C. Multi-Terminal Memtransistor from Polycrystalline Monolayer Molybdenum Disulfide. *Nature* **2018**, *554*, 500−504.
(25) Zhao, M.; Ye, Y.; Han, Y.; Xia, Y.; Zhu, H.; Wang, S.; Wang, Y.; Muller, D. A.; Zhang, X. Large-Scale Chemical Assembly of Atomically Thin Transistors and Circuits. *Nat. Nanotechnol.* **2016**, *11*, 954−959.
(26) Sun, D.; Nguyen, A. E.; Barroso, D.; Zhang, X.; Preciado, E.; Bobek, S.; Klee, V.; Mann, J.; Bartels, L. Chemical Vapor Doposition Growth of a Periodic Array of Single-Layer MoS_2 Islands *via* Lithographic Patterning of an SiO_2/Si Substrate. *2D Mater.* **2015**, *2*, 045014.
(27) Bruix, A.; Fuchtbauer, H. G.; Tuxen, A. K.; Walton, A. S.; Andersen, M.; Porsgaard, S.; Besenbacher, F.; Hammer, B.ør.; Lauritsen, J. V. *In Situ* Detection of Active Edge Sites in Single-Layer MoS_2 Catalyst. *ACS Nano* **2015**, *9*, 9322−9330.
(28) Eaglesham, D. J.; Cerullo, M. Dislocation-Free Stranski-Krastanow Growth of Ge on Si(100). *Phys. Rev. Lett.* **1990**, *64*, 1943−1946.
(29) Rice, C.; Young, R. J.; Zan, R.; Bangert, U.; Wolverson, D.; Georgiou, T.; Jalil, R.; Novoselov, K. S. Raman-Scattering Measurements and First-Principles Calculations of Strain-Induced Phonon Shifts in Monolayer MoS_2. *Phys. Rev. B: Condens. Matter Mater. Phys.* **2013**, *87*, No. 081307.
(30) Kukucska, G.; Koltai, J. Theoretical Investigation of Strain and Doping on the Raman Spectra of Monolayer MoS_2. *Phys. Status Solidi B* **2017**, *254*, 1700184.
(31) You, H. Angle Calculation for a '4S+2D' Six-Circle Diffractometer. *J. Appl. Crystallogr.* **1999**, *32*, 614−623.
(32) Kresse, G. J.; Furthmüller, J. Efficient Iterative Schemes for *Ab Initio* Total-Energy Calculations Using a Plane-Wave Basis Set. *Phys. Rev. B: Condens. Matter Mater. Phys.* **1996**, *54*, 11169−11186.
(33) Malyi, O. I.; Kulish, V. V.; Persson, C. In Search of New Reconstruction of (001) a-Quartz Surface: A First Principles Study. *RSC Adv.* **2014**, *4*, 55599−55603.
(34) Smithe, K. K. H.; Suryavanshi, S. V.; Munoz Rojo, M.; Tedjarati, A. D.; Pop, E. Low Variability in Synthetic Monolayer MoS_2 Devices. *ACS Nano* **2017**, *11*, 8456−8463.
(35) Zhang, J.; Yu, H.; Chen, W.; Tian, X.; Liu, D.; Cheng, M.; Xie, G.; Yang, W.; Yang, R.; Bai, X.; Shi, D.; Zhang, G. Scalable Growth of

https://dx.doi.org/10.1021/acsnano.0c00132
ACS Nano 2020, 14, 6570−6581

High-Quality Polycrystalline MoS_2 Monolayers on SiO_2 with Tunable Grain Sizes. *ACS Nano* **2014**, *8*, 6024−6030.
(36) Perdew, J. P.; Burke, K.; Ernzerhof, M. Generalized Gradient Approximation Made Simple. *Phys. Rev. Lett.* **1996**, *77*, 3865−3868.
(37) Blöchl, P. E. *Phys. Rev. B: Condens. Matter Mater. Phys.* **1994**, *50*, 17953−17979.
(38) Henkelman, G.; Arnaldsson, A.; Jonsson, H. A Fast and Robust Algorithm for Bader Decomposition of Charge Density. *Comput. Mater. Sci.* **2006**, *36*, 354−360.

https://dx.doi.org/10.1021/acsnano.0c00132
ACS Nano 2020, 14, 6570−6581